Sample dispersion in isotachophoresis: supplementary material

G. GARCIA-SCHWARZ, M. BERCOVICI, L. A. MARSHALL and J. G. SANTIAGO

A. Derivation of internal pressure gradients due to non-uniform EOF

The bulk electroosmotic flow (EOF) in a channel, $\bar{U}_{EOF}$, is equal to the axial-average electroosmotic (EO) slip. If we account for differences in EO mobility between the LE and TE (due to differences in pH and/or ionic strength), then we find

$$\bar{U}_{EOF} = \left(\frac{L_{TE}}{L}\right)\mu_{EOF}^{TE} E_{TE} + \left(1 - \frac{L_{TE}}{L}\right)\mu_{EOF}^{LE} E_{LE}\,. \qquad \text{(A.1)}$$

Here L_{TE} is the length of the TE zone, L is the total channel length, μ_{EOF}^{TE} and μ_{EOF}^{LE} are the EO mobilities in the TE and LE, and E_{TE} and E_{LE} are the electric field values in the TE and LE. The superscripts "TE" and "LE" indicate the zone in which the EO mobility is evaluated. We assume that non-uniform EOF results in locally-uniform pressure gradients sufficiently far from the ITP boundary. Azimuthally-uniform flow within a circular channel gives the well-known Poiseuille flow result,

$$u_i(r) = \frac{1}{4\eta}\left.\frac{\partial p}{\partial z}\right|_i r^2 + A_i \ln(r) + B_i\,. \qquad \text{(A.2)}$$

Here u_i is the axial fluid velocity, η is the fluid dynamic viscosity, p is the pressure, and A_i and B_i are constants of integration. We require that (A.2) satisfy the EO slip velocity at the channel walls and we also require the solution to remain finite at the channel centerline,

$$u_i(r = R) = \mu_{EOF}^{i} E_i\,, \qquad u_i(r = 0)\ \ bounded\,. \qquad \text{(A.3)}$$

In formulating these boundary conditions we make the assumption that the difference in hydrodynamic pressure between both channel reservoirs is negligible, so that there is no external pressure driven flow in the channel. We then impose these boundary conditions and find

$$u_i(r) = \frac{1}{4\eta}\left.\frac{\partial p}{\partial z}\right|_i \left(r^2 - R^2\right) + \mu_{EOF}^{i} E_i\,. \qquad \text{(A.4)}$$

We integrate $u_i(r)$ in r and θ, which allows us to express the pressure gradient in each zone as a function of the flow rate, Q,

$$\left.\frac{\partial p}{\partial z}\right|_i = \frac{8\eta}{R^2}\left(\frac{Q}{\pi R^2} - \mu_{EOF}^i E_i\right). \quad \text{(A.5)}$$

The flow rate is defined as $Q \equiv \pi R^2 \bar{U}_{EOF}$, where $\bar{U}_{EOF}$ is given in (A.1). We note that the ITP condition requires the electric fields in the LE and TE to be related by a ratio of electrophoretic mobilities, $E_{TE} = (\mu_{LE} / \mu_{TE}) E_{LE}$. Simplifying (A.5) with these results we find

$$\left.\frac{\partial p}{\partial z}\right|_{TE} = -\frac{8\eta}{R^2} E_{LE}\left(\mu_{EOF}^{LE} - \gamma\mu_{EOF}^{TE}\right)\left(1 - \frac{L_{TE}}{L}\right), \quad \text{(A.6}a\text{)}$$

$$\left.\frac{\partial p}{\partial z}\right|_{LE} = \frac{8\eta}{R^2} E_{LE}\left(\mu_{EOF}^{LE} - \gamma\mu_{EOF}^{TE}\right)\left(\frac{L_{TE}}{L}\right), \quad \text{(A.6}b\text{)}$$

where $\gamma = \mu_{LE}/\mu_{TE}$. The difference in magnitude between the LE and TE pressure gradients is then:

$$\left.\frac{\partial p}{\partial z}\right|_{TE} - \left.\frac{\partial p}{\partial z}\right|_{LE} = -\frac{8\eta}{R^2} E_{LE}\left(\mu_{EOF}^{LE} - \gamma\mu_{EOF}^{TE}\right). \quad \text{(A.7)}$$

For the constant applied current considered here, E_{LE} is a constant, and so this difference in pressure gradient is constant in time.

B. Scaling and perturbation analysis for electroneutrality approximation

We consider a sample species focusing in peak mode ITP with leading (LE), trailing (TE), counterion (CI), and sample (A) ions.

Gauss' law in differential form is

$$\nabla \cdot (\varepsilon E) = F \sum_i z_i c_{i,z_i}, \quad \text{(B.1)}$$

where ε is the permittivity, E is the electric field, F is the Faraday constant, and z_i and c_i are the valence and concentration of species i, respectively. Assuming a constant permittivity and one-dimensional domain for simplicity, then

$\varepsilon \frac{dE}{dx} = F \sum_i z_i c_{i,z_i}$.	(B.2)

We scale the dependent variables (electric field and species concentrations) as follows:

$\frac{dE}{dx} \sim \frac{E_{LE} - E_{TE}}{\delta} = \frac{\Delta E}{\delta}$,	(B.3)
$c_{i,z_i} \sim c_0$, for $i = \{LE, TE, CI, A\}$	(B.4)

Here E_{LE} *and* E_{TE} are the uniform electric fields in the LE and TE regions, respectively, δ is the width of the ITP interface, and c_0 is the initial LE concentration.

Applying (B.3) and (B.4) to equation (B.2), for ITP with monovalent species we find

$-\left(\frac{\varepsilon \Delta E / F c_0}{\delta} \right) \frac{dE}{dx} = c_{LE,-1} + c_{TE,-1} - c_{CI,+1} + c_{A,-1}$.	(B.5)

We identify the smallness parameter in (B.5) as the ratio of the electric (Debye) length-scale ($\ell_{electric}$) to the length-scale associated with the ITP interface (ℓ_{ITP}),

$\xi \equiv \frac{\varepsilon \Delta E / F c_0}{\delta} = \frac{\ell_{electric}}{\ell_{ITP}} \sim 10^{-5} - 10^{-6}$	(B.6)

In evaluating the smallness parameter, we assume typical parameter values for ITP buffers and experiments (see Table S2 in Appendix D for values corresponding to experiments done in this study). We use the result derived by MacInnes & Longsworth (1932) for the characteristic width of the boundary between two ITP zones, δ, see (F.1).

We expand all dependent variables with respect to this parameter

$E = E^{(0)} + \xi E^{(1)} + \xi^2 E^{(2)} + \ldots$,	(B.7)
$c_{i,z_i} = c_{i,z_i}^{(0)} + \xi c_{i,z_i}^{(1)} + \xi^2 c_{i,z_i}^{(2)} + \ldots$,	(B.8)

and substitute equations (B.7) and (B.8) in equation (B.5) to find the zeroth and first order equations

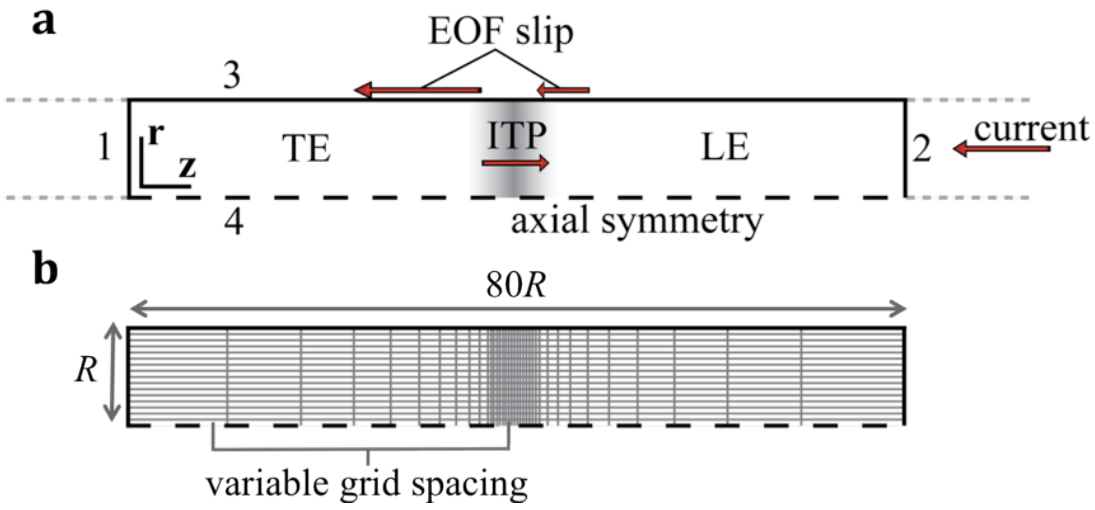

FIGURE S1. Schematic of computational domain for numerical simulations of ITP with non-uniform electroosmotic flow. (*a*) The computational domain consists of an isolated portion of the microchannel moving in the frame of reference of the focused sample. Arrows denote the direction of ITP migration and EOF, with arrow lengths showing the relative strength of EO slip in the LE and TE zones. The boundary numbering corresponds to boundary conditions listed in Table S1. The dashed line on boundary 4 denotes the axis of symmetry. (*b*) Schematic of the domain discretization scheme. We use a uniform discretization in the radial dimension. In the axial dimension, we concentrate grid elements in the region occupied by the focused sample and the LE-TE interface, with an average grid element size of 0.5 μm. Away from this interface and towards boundaries 1 and 2 the average grid element size is approximately 5 μm on average.

$$\xi^0\left(c_{LE,-1}^{(0)}+c_{TE,-1}^{(0)}-c_{CI,+1}^{(0)}+c_{A,-1}^{(0)}\right)+\xi^1\left(c_{LE,-1}^{(1)}+c_{TE,-1}^{(1)}-c_{CI,+1}^{(1)}+c_{A,-1}^{(1)}+\frac{dE^{(0)}}{dx}\right)+\ldots=0\,. \tag{B.9}$$

Evidently the zeroth order equation is simply the electroneutrality approximation

$$c_{LE,-1}^{(0)}+c_{TE,-1}^{(0)}-c_{CI,+1}^{(0)}+c_{A,-1}^{(0)}=0\ . \tag{B.10}$$

In peak mode ITP we have the additional constraint that $c_A \ll c_0$. In this case, we can express the eletroneutrality approximation for peak mode ITP as

$$c_{LE,-1}^{(0)}+c_{TE,-1}^{(0)}-c_{CI,+1}^{(0)}=0\,. \tag{B.11}$$

C. Boundary conditions and discretization of numerical domain

Figure S1 shows a schematic of the computational domain for our numerical simulations. Only a portion of the full microchannel, shown in figure S1(*a*) is modeled and discretized in numerical simulations. Far from the LE-TE interface, we assume that the LE and TE zones reach a steady state that can be modeled using constant concentration boundary conditions. Boundaries 1 and 2 represent the ends of the modeled domain, boundary 3 is the channel wall, and boundary 4 is the channel centerline (axis of symmetry). The boundary conditions are summarized in table S1. We use a computationally-efficient domain discretization, shown in figure S1(*b*), in which we discretize the domain uniformly in the radial dimension while concentrating elements near the ITP interface in the axial dimension. Again, we stress that this discretization only holds under the assumption that the domain reaches a steady state far from the LE-TE boundary.

TABLE S1 Summary of the boundary conditions used in our numerical simulations. We assume constant applied current. The velocity of the frame of reference (relative to the laboratory frame) is $U_{zone} = U_{ITP} + \bar{U}_{EOF}$. The electromigration flux and species flux are denoted J_ϕ and J_S. The constants c_{LE}^0 and c_{TE}^0 denote the initial LE and TE zone concentrations, respectively. Boundary numbering corresponds to the schematic of the computational domain shown in figure S1(*a*).

Boundary	Velocity/pressure	Current/potential	Concentration
1	velocity: $u(r) = u_{TE}(r) - U_{zone}$	const. potential: $\phi(r) = 0$	const. concentration: $c_{LE}(r) = 0$, $c_{TE}(r) = c_{TE}^0$, $c_A(r) = 0$
2	const. pressure: $p(r) = 0$	const. current density: $j(r) = j_{applied}$	const. concentration: $c_{LE}(r) = c_{LE}^0$, $c_{TE}(r) = 0$, $c_A(r) = 0$
3	EO slip: $u(z) = \mu_{EOF}(z)E(z,R)$	insulation: $n \cdot J_\phi = 0$	zero net flux: $n \cdot J_s = 0$
4	Axisymmetric: $\frac{\partial u}{\partial r} = 0$, $\frac{\partial v}{\partial r} = 0$	Axisymmetric: $n \cdot J_\phi = 0$	Axisymmetric: $n \cdot J_s = 0$

D. Simulation parameters

The parameter values used in our simulations are summarized in Table S2. We express all electrolyte properties in terms of effective mobilities and total concentrations. The local mobility of partially-ionized weak electrolytes in the problem (here TE and CI) are a function of local pH. We model this pH dependence of TE ion and CI ion mobility by interpolating based on the total LE and TE ion concentrations

$$\mu_i = \frac{\mu_i^{TE} c_{TE} + \mu_i^{LE} c_{LE}}{c_{TE} + c_{LE}} . \qquad \text{(D.1)}$$

Here, the subscript *i* denotes the ion of interest (TE or CI). This function only approximates the detailed physics governing pH dependence, but does capture the correct trend: the effective mobility of analyte *i* approaches μ_i^{TE} in the TE zone and μ_i^{LE} in the LE zone. As shown in table S2, the latter two values for the TE ions are respectively 18.22 and 15.71 x 10^{-9} $m^2V^{-1}s^{-1}$.

We use the same interpolation as in (D.1) to estimate the variation of electroomostic slip between LE and TE zones. pH-dependence of the LE ion and Alexa Fluor 488 was not accounted for, as we used a strong acid (HCl) as our LE ion and chose the pH of our buffer chemistry to be far from the pKa of Alexa Fluor 488. The effective mobilities of Alexa Fluor 488 and Fluorescein are listed in Table S2 and discussed in the main text.

TABLE S2. Parameter values used in numerical simulations of ITP with non-uniform EOF

Description	**Symbol**	**Value(s) used in simulations**	**Comments**
LE ion total concentration – LE zone	c_{LE}	100 mM	Chloride ions; 100 mM Tris-HCl buffer
TE total concentration – TE zone	c_{TE}	66.1 mM	MES ions; adjusted Tris-MES buffer; determined by KRF (Kohlrausch 1897)
CI total concentration – LE zone	c_{CI}	200 mM	CI concentration in TE adjusts according to KRF (Kohlrausch 1897)
LE effective mobility	μ_{LE}	-68.5E-9 m^2 V^{-1} s^{-1}	Chloride ions in LE buffer; HCl is a strong acid, and its mobility is assumed constant throughout the domain
TE effective mobility - TE zone	μ_{TE}^{TE}	-18.22 m^2 V^{-1} s^{-1}	MES ions in adjusted TE buffer
TE effective mobility – LE	μ_{TE}^{LE}	-15.7 x 10^{-9} m^2 V^{-1} s^{-1}	MES ions in LE buffer

zone			
CI effective mobility – TE zone	μ_{CI}^{TE}	6.60 x 10^{-9} m^2 V^{-1} s^{-1}	Tris ions in adjusted TE buffer
CI effective mobility – LE zone	μ_{CI}^{LE}	8.99 x 10^{-9} m^2 V^{-1} s^{-1}	Tris ions in LE buffer
Analyte effective mobility	μ_A	-29.5 x 10^{-9} m^2 V^{-1} s^{-1} (AF488), -18.9 x 10^{-9} m^2 V^{-1} s^{-1} (Fluorescein)	--
EO mobility (LE)	μ_{EOF}^{LE}	~19 x 10^{-9} m^2 V^{-1} s^{-1}	Varies ±10% by experiment
EO mobility (TE)	μ_{EOF}^{TE}	~19 x 10^{-9} m^2 V^{-1} s^{-1}	Varies ±10% by experiment
Relative permittivity	ε_r	75	Estimated for LE and TE buffers based on relative permittivity of water and dilute HCl solutions

E. Simulating optical diffraction effects with a three-dimensional point spread function

In order to aid in the comparison of experimental and simulation data, we consider the effects of optical diffraction introduced into experimental data by the microscope objective. Objectives have a specific three-dimensional point spread function (PSF) that describes the response of the objective to a point stimulus. For simplicity, we approximate a microscope objective as a single Gaussian lens with finite aperture; under this assumption the PSF is described analytically by Lommel functions (Born & Wolf 1964). The shape of the PSF depends only on the following properties: the wavelength of light being imaged (λ), the index of refraction of the medium (n), and the objective's numerical aperture (NA), working distance (WD), and magnification (M).

Born and Wolf (1964) show that the light intensity associated with a converging spherical wave emitted from a finite aperture is given by

$$I(u,v)=\left(\frac{2}{u}\right)^2\left[U_1^2(u,v)+U_2^2(u,v)\right]I_0, \qquad \text{(E.1)}$$

where,

$$u\equiv\frac{2\pi}{\lambda}\left(\frac{a}{f}\right)^2 z,$$

$$v = \frac{2\pi}{\lambda}\left(\frac{f}{a}\right) r\,,$$

$$I_0 \equiv \left(\frac{\pi a^2 A}{\lambda f^2}\right)^2,$$

$$U_n(u,v) \equiv \sum_{s=0}^{\infty} (-1)^s \left(\frac{u}{v}\right)^{n+2s} J_{n+2s}(v).$$

Here a is the aperture radius, f is the axial distance from the objective to the image plane, λ is wavelength of the fluorescence emission, z is the distance from the focal plane in the direction towards or away from the objective, r is the radial dimension, A is an arbitrary scaling constant, u and v are dimensionless coordinates in the image plane, and J_k denotes the Bessel function of order k. We calculate the theoretical aperture radius, a, using the thin lens approximation $NA \approx na / f$.

Figure S2(a) shows the centerline log-intensity of the PSF corresponding to a 20x objective with 0.5 numerical aperture (NA) and 2.1 mm working distance (WD) and found using this method. These are the characteristics of the objective used in ITP experiments focusing Alexa Fluor 488 presented in the main text (see §5). Convolution of this PSF with numerical data approximates the diffraction effect of this objective in experiments. In order to perform the convolution, we first construct a three-dimensional scalar field from the two-dimensional axisymmetric numerical simulation data. Then, based on the z discretization of our data (here 0.2 μm), we determine the two-dimensional PSF corresponding to each plane (here a fixed value of u). We then convolve each x-y plane of our three-dimensional scalar data with the corresponding x-y plane of the three-dimensional PSF. Finally, we perform a line-of-sight integration to produce images which can be compared to experimental visualizations.

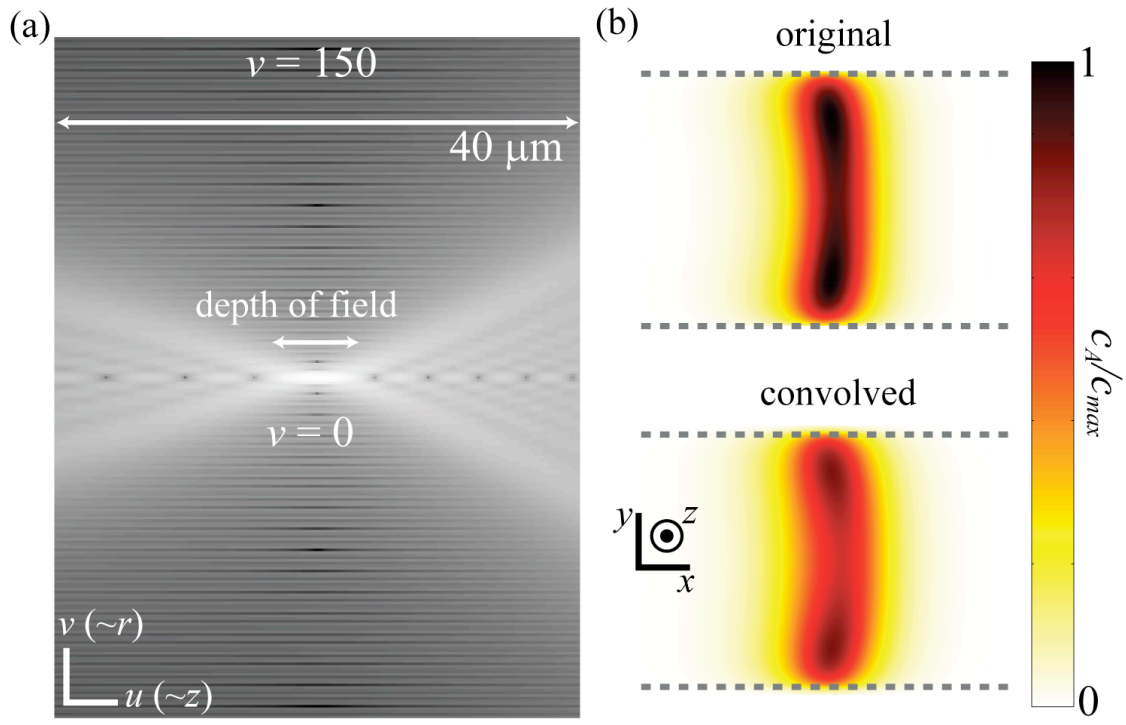

FIGURE S2. Effect of optical diffraction on numerical data. (a) Log-intensity image of the theoretical three-dimensional PSF of an Olympus UPlanFl 20x objective with 0.5 NA and 2.1 mm WD modeled as a thin Gaussian lens. The extents of the image correspond to -150 < v < 150 and the full diameter (40 μm) of the capillary in the u dimension. (b) Comparison of line-of-sight-averaged numerical data without post-processing ("original") and after convolution ("convolved") with the PSF shown in (a). The convolution step results in a significant decrease in signal intensity.

Figure S2(*b*) shows a comparison of original and optically-adjusted simulation images. Here the "original" is a simple line-of-sight (along z-axis) integration of the axisymmetric scalar from the computation. The image labeled "convolved" in addition has a convolution with the three-dimensional PSF function performed before the line-of-sight integration. This latter image approximates the optical effects of the objective. While the shape of the plug is not significantly altered by the convolution, we do see a significant decrease in maximum intensity, in particular near the channel centerline. As expected, the convolution also results in some scalar intensity outside the channel boundaries, thereby slightly increasing the vertical (along y-axis) height of the original scalar. In this convolution (and

all optically-adjusted images presented in this study) we assume that the focal plane coincides with the central capillary plane. Because the PSF for this objective is narrowest within a 3 μm region around the focal plane, we expect the central plane to be emphasized in the convolved images. Indeed, this is the reason we see much clearer near-wall sample accumulation in the convolved image in figure S2(*b*) than in the original.

F. Prefactor for ITP boundary width

The width of the LE-TE interface was first studied analytically by MacInnes & Longsworth (1932), who found that this width, δ, scales inversely with current density,

$$\delta \equiv \frac{4\sigma_{LE} k_b T}{ej} \frac{\mu_{TE}}{\mu_{LE} - \mu_{TE}}. \quad \text{(F.1)}$$

Here σ_{LE} is the conductivity of the leading electrolyte, k_b is the Boltzmann constant, T is the temperature, e is the electron charge, μ_{TE} is the mobility of the trailing ion, and μ_{LE} is the mobility of the leading ion. We use this result in our approximations of the ITP electric field at the LE-TE interface. These approximations (presented in §4) can be interpreted as first-order Taylor series expansions of the electric field in the three regions shown in figure S3: the LE zone (region A), the TE zone (region C), and the LE-TE interface (region B). In regions A and C the ion concentration and zone conductivity are uniform. These regions therefore have uniform electric field determined by the local conductivity, $E_i = j / \sigma_i$. In region B, we model the electric field as linear and do not account for dispersion. In this region, the electric field varies monotonically from its value in the TE to its value in the LE. We hypothesize that the maximum gradient scales inversely with the non-dispersed interface width (δ) as follows:

$$\nabla E_{\max} = \left(\frac{E_{TE} - E_{LE}}{a\delta} \right). \quad \text{(F.2)}$$

Here $\nabla E_{\max}$ is the maximum gradient in electric field, E_{LE} is the electric field in the LE, E_{TE} is the electric field in the TE, and a is an unknown prefactor. This maximum gradient corresponds to the electric field's point of inflection. In our model, we choose $\nabla E_{\max}$ as the slope of the linear field region. Figure S3 presents this approximation against the ITP electric field distribution from a one-dimensional numerical simulation (described below).

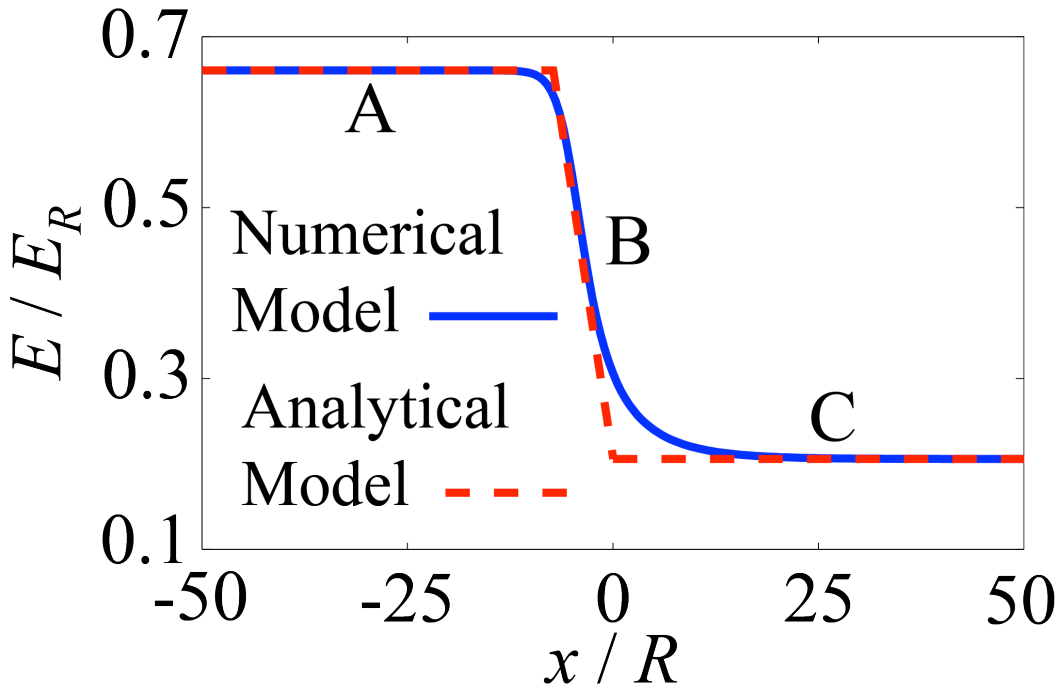

FIGURE S3. Comparison of numerical prediction of electric field (solid) versus analytical model approximations used here (dashed). We use a one-dimensional steady-state numerical simulation of ITP to find the electric field in the LE zone, LE-TE interface region, and TE zone. We denote these as regions C, B, and A, respectively. We model the electric field as uniform in regions A and C and linearly varying in region B.

Using (F.2) we can solve for the prefactor,

$$a = \frac{E_{TE} - E_{LE}}{\nabla E_{\max} \delta}. \qquad \text{(F.3)}$$

In this relation, the LE and TE electric fields and the interface width scaling are known analytically. The interface length scale δ is taken from the MacInnes model, as in (F.1). The only unknown quantity in this relation is the maximum electric field gradient.

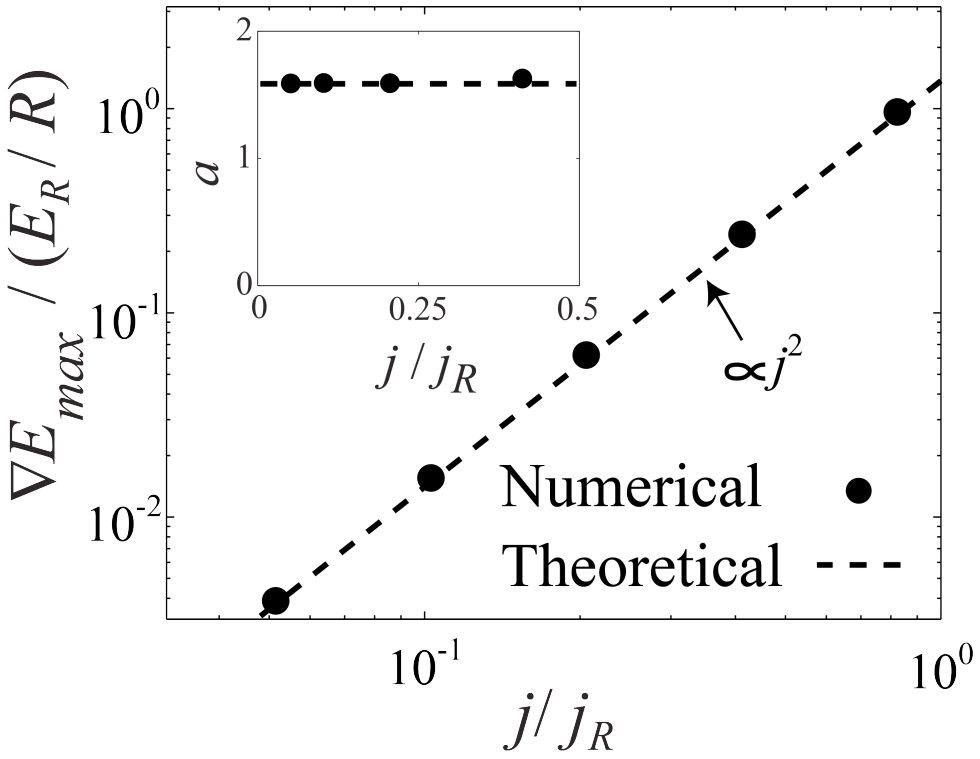

FIGURE S4 Maximum value of the electric field gradient, ∇E_{max} over a range of applied current densities calculated using a one-dimensional simulation. These simulations show that the electric field gradient is proportional to the square of the applied current density, as predicted by the interface width relation derived by MacInnes & Longsworth (1932). The inset shows the value of the prefactor, *a*, determined from each of the data points shown in the main plot. The value of the prefactor is uniform across a wide range of current density, which suggests that the maximum electric field gradient also follows the MacInnes relation. The value of this prefactor, *a*, is approximately 1.58.

We develop a one-dimensional numerical simulation to determine the value of the maximum electric field gradient. We follow a method similar to that presented by Khurana *et al.* (2008) to numerically model (non-dispersed) peak mode ITP. The conservation equation governing the problem of one-dimensional electromigration and diffusion in a cylindrical channel written in the frame of reference of the moving ITP zone (U_{ITP}) and neglecting bulk flow is

$$\frac{\partial c_i}{\partial t} - U_{ITP}\frac{\partial c_i}{\partial x} = \frac{\partial}{\partial x}\left(-\mu_i c_i E + D_i \frac{\partial c_i}{\partial x}\right). \quad \text{(F.4)}$$

Here c_i is the concentration of ion species i, U_{ITP} is the velocity of the ITP zone, μ_i is the electrophoretic velocity of species i, and E is the electric field.

We use current conservation to solve for electric field,

$$E = \frac{j}{\sigma} - \frac{F}{\sigma}\left(\sum_i z_i D_i \frac{\partial c_i}{\partial x}\right). \quad \text{(F.5)}$$

We solve these equations numerically in MATLAB using the parabolic partial differential equation (PDE) solver (the "pdepe" function) using constant concentration boundary conditions. For the TE boundary concentration we use the value predicted by the Kohlrausch regulating function (Kohlrausch 1897). For a steady-state solution, the PDEs were allowed to evolve in time until convergence.

Figure S4 shows calculated values of $\nabla E_{\max}$ over a range of applied current densities. From equation (F.1) we see that the interface width scales inversely with applied current density, $\delta \propto 1/j$. Note also that far from the LE-TE interface, the electric field is determined only by current density and conductivity. The difference between the LE and TE electric fields is therefore linearly proportional to current density,

$$\Delta E = \frac{j}{\sigma_{TE}} - \frac{j}{\sigma_{LE}} \propto j. \quad \text{(F.6)}$$

Together, this suggests that the electric field gradient grows with the square of the current density:

$$\nabla E_{\max} \propto \frac{\Delta E}{\delta} \propto j^2. \quad \text{(F.7)}$$

The numerical data in figure S4 agrees with this theoretical prediction.

The inset to figure S4 shows the calculated value of the prefactor, a, using (F.3) for a range of applied current densities. Note that the value of this prefactor ($a \approx 1.58$) is independent of applied current density in the range of interest.

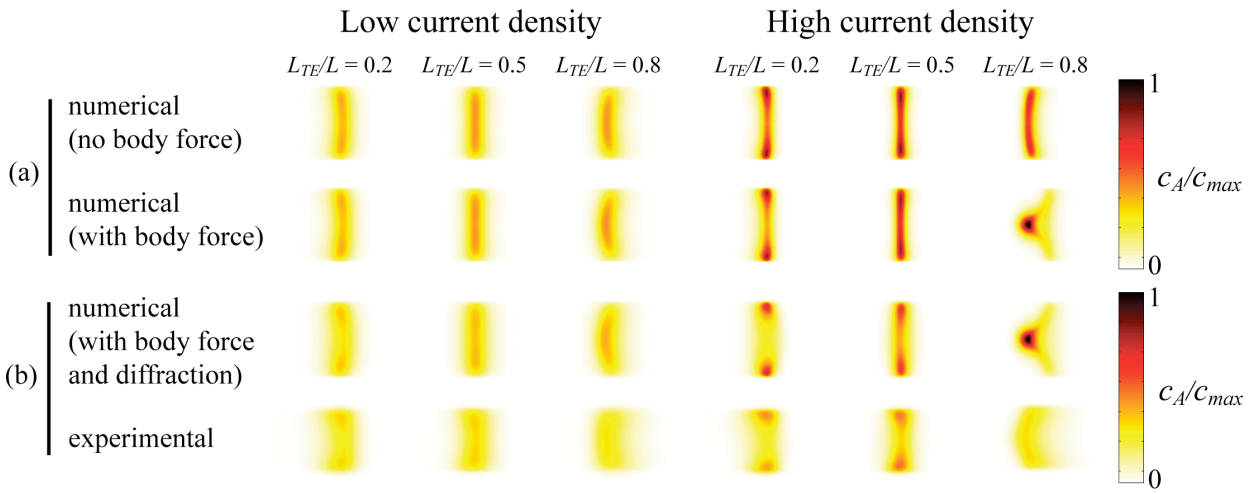

FIGURE S5. Effect of including the body force on simulation predictions and their comparison with experimental observations for relatively low (left, $j/j_R = 3.13$) and high (right, $j/j_R = 6.26$) current densities. The first three rows show numerical results and the fourth row is experimental data. All image intensities are normalized by the intensity volume integral, and colorbar scalings are then chosen to maximize dynamic range of the collection. For clarity of presentation, colorbar normalization differs between (*a*) and (*b*) (the intensities of the data in (*b*) are slightly lower). For all experiments, we used a 20X objective with 0.5 numerical aperture and 10 ms exposure time in a 40 μm inner diameter capillary. (*a*) Line-of-sight-averaged numerical results for simulations with and without the body force term in the momentum equation. Inclusion of body force has negligible effect at low current density. At high current density, including body force results in stronger radial redistribution of analyte (particularly near centerline accumulation near the LE boundary). (*b*) Comparison of simulations including body force with experiments. We adjusted the raw numerical results accounting for the body force by convolving with a 3D point response function to account for optical diffraction, as described in Appendix E. The only significant disagreement between experiments and numerics occurs for the $L_{TE}/L = 0.8$ observation in the high current density case. Simulations predict strong near-centerline sample accumulation while experiments show a uniform distribution more comparable to simulations neglecting body force. We believe this discrepancy may be due to flow instabilities not captured by our axisymmetric numerical model.

G. Inclusion of the electric body force in numerical simulations

In our simulations, we included the electric body force in the momentum equations. Sounart & Baygents (2007) developed a lubrication theory applicable to electrokinetic flow with axial conductivity gradients that includes the effects of electrohydrodynamic body

forces. However, to our knowledge ours is the first study to include body forces in simulations of ITP. Schönfeld *et al.* (2009) argued that the axial pressure gradients produced by the body force acting on charge stored at the ITP interface is negligible when compared to the internal pressure gradients generated by non-uniform EOF. While this may be true, their formulation does not consider the magnitude of the radial body force when compared to radial pressure forces acting at the ITP interface.

We find that inclusion of the electric force can lead to a significant effect on simulation predictions for the case of relatively high applied current density. Figure S5 shows simulations with and without the electric body force. At high current densities (j/j_R greater than about 5.3), including the body force leads to strong central sample accumulation in the $L_{TE}/L > 0.5$ region (images for $L_{TE}/L = 0.8$ are shown in Figure S5), while simulations without the body force predict a more uniform radial distribution. In contrast, the body force seems to have very little effect for current densities below about 0.7 A cm^{-2} (near $j/j_R = 4.5$) which are more typical of ITP assays.

Experimental observations do not corroborate this dramatic central accumulation predicted by simulations with body forces at high current density. In fact, exclusion of the body force leads to better qualitative agreement for high current density. The reasons for this discrepancy are not clear. However, we do note that experimentally we observe flow instabilities in the ITP interface for current densities above 0.8 A cm^{-2} (roughly j/j_R greater than about 5.3). Such flow instabilities were observed experimentally by Persat & Santiago (2009) and modeled by Santos & Storey (2008) in their numerical work on electrokinetic instabilities due to streamwise conductivity gradients. Beginning at current densities of about 0.8 A cm^{-2}, we observe steady azimuthal asymmetries in experiments. Above 2 A cm^{-2} we sometimes observe strong temporal fluctuations in the scalar fields. We hypothesize that the onset of flow instabilities at higher current densities may account for the discrepancies between predictions and experimental observations. Our simulations are axisymmetric, and so our model cannot capture azimuthal variations. We recommend that investigations of high electric field cases use fully three-dimensional, unsteady simulations, and that they include the electric body force term. Such an approach may help resolve the effects of electric body forces at high currents.

References

BORN, M. & WOLF, E. 1964 *Principles of optics: Electromagnetic theory of propagation, interference and diffraction of light*. Macmillan.

KHURANA, T. K., SANTIAGO, J. G. 2008 Sample zone dynamics in peak mode isotachophoresis. *Anal. Chem.* **80** (16), 6300–6307.

KOHLRAUSCH, F. 1897 Über concentrations-verschiebungen durch electrolyse im inneren von lösungen und lösungsgemischen. *Ann. Physik* **298** (10), 209–239.

MACINNES, D. A. & LONGSWORTH, L. G. 1932 Transference numbers by the method of moving boundaries. *Chem. Rev.* **11** (2), 171–230.

PERSAT, A. & SANTIAGO, J. G. 2009 Electrokinetic control of sample splitting at a channel bifurcation using isotachophoresis. *New J. Phys.* **7**, 075026.

SCHÖNFELD, F., GOET, G., BAIER, T. & HARDT, S. 2009 Transition zone dynamics in combined isotachophoretic and electro-osmotic transport. *Phys. Fluids* **21** (9), 092002.

SANTOS, J. J. & STOREY, B. D. 2008 Electrokinetic instability of electro-osmotic channel flow with streamwise conductivity gradients. *Phys. Rev. E* **78**, 046316.

SOUNART, T. L. & BAYGENTS, J. C. 2007 Lubrication theory for electro-osmotic flow in a non-uniform electrolyte. *J. Fluid Mech.* **576**, 139–172.